Three-phase CFD-DEM study on the hydrodynamics of a riser system with liquid injection

Chemical Engineering Journal 501 (2024) 157449

Contents lists available at ScienceDirect

Chemical Engineering Journal

journal homepage: www.elsevier.com/locate/cej

Three-phase CFD-DEM study on the hydrodynamics of a riser system with liquid injection

Juan G. Ramírez, Levi Peene, Maike Baltussen *, Kay Buist, Johannes A.M. (Hans) Kuipers

Multiphase Reactors Group, Department of Chemical Engineering & Chemistry, Eindhoven University of Technology, Eindhoven, 5600 MB, The Netherlands

ARTICLE INFO

Keywords:
CFD-DEM
Liquid injection
Particle-droplet collision
Wet particles
Riser
Clustering

ABSTRACT

Riser reactors are frequently applied in the process industry for highly important catalytic processes. In this work, a computational fluid dynamics-discrete element method (CFD-DEM) for a riser with liquid injection was developed. This model treats the gas as a continuous phase whereas the liquid droplets and catalyst particles are treated as discrete elements. The presence of droplets causes particles to be wet, which is taken into account via coverage models of the particles. In addition, the liquid on the particles will change the collision behavior, which is included using an energy balance approach. This CFD-DEM study is conducted simulating a lab-scale pseudo-2D riser. Based on the comparison, the assumption of fully covered particles results in a significant increase in the solids holdup and clustering behavior of the riser which, especially at the low liquid flow rate, results in an over-prediction. The partial coverage simulations show that only half of the particles are covered, which has a major effect on the collisions.

1. Introduction

Risers are a reactor type that perform important catalytic processes such as base chemical production, biomass gasification and fluid catalytic cracking [1–3]. Generally a riser consists of a long tube in which the catalyst particles are injected from the bottom. In addition, air is provided at the bottom of the reactor to convey the particles along the riser with a residence time typically lower than 10 seconds [3]. Above the feeding point of the catalyst particles, liquid reactants can be injected via nozzles as fine droplets that can react with the catalyst after evaporation. Despite the geometrical simplicity, the interaction of the three phases leads to operational challenges. A well-known challenge is the heterogeneous structure of the solid phase resulting from the formation of clusters. These clusters lead to phenomena as solid back mixing and poor heat and mass transfer between the phases [1,4–7]. Aiming to mitigate these phenomena, multiple experimental and numerical studies have been performed to improve the operational conditions.

Among the numerical studies, two common modeling approaches are used. The first is the Computational Fluid Dynamics-Discrete Element Method (CFD-DEM) approach. This model tracks each catalyst particle individually using Newton's second law, while the gas phase is treated as a continuous phase solving the Navier–Stokes and continuity equations. Because of the high computational demand due to the need to follow every particle separately and resolving the interactions between them, this approach is limited to lab-scale risers [8–11]. The second approach, the Two Fluid Model (TFM), treats both gas and solid as continuous phases and the solids interactions are grouped in continuous variables such as solids stress and solids viscosity. This approach has a significantly lower computational demand and can therefore be used to study industrial-size units [12–14]. All the aforementioned studies do not include the liquid phase inside the riser most probably assuming a fast vaporization of the liquid droplets inside the riser. Although this is true for small droplets (~100 micrometers) as the vaporization time is approximately 0.06 s [15], atomization can lead to droplets of 2000 micrometers. The evaporation time of these large droplets (~0.06 s) is comparable to the residence time of particles in the riser [16].

In an attempt to prove the relevance of the liquid phase, Gao et al. [17] determined for an industrial scale riser, the difference between the predictions of the gas–solid approach with the gas–liquid–solid approach. Despite the considerable effect of the liquid phase on the reaction yield, there is no discussion on the effect of the liquid phase on the hydrodynamics of the riser, particularly the heterogeneity of the solids phase and cluster formation. An effect on the particle structures is expected as compared to dry collisions because the viscous and capillary forces increase the dissipation of energy in wet collisions. In addition, the injection of a liquid changes the global hydrodynamics for particle systems as spouted [18] and conventional [19] fluidized beds.

* Corresponding author.
E-mail address: m.w.baltussen@tue.nl (M. Baltussen).

https://doi.org/10.1016/j.cej.2024.157449

Available online 13 November 2024

Nomenclature

Roman symbols

a	shape parameter of Weibull radius distribution
b	scale parameter of Weibull radius distribution
D	minimum half separation distance between the surface of colliding particles, m
d_p	particle diameter, m
e_n	normal restitution coefficient
e_t	tangential restitution coefficient
$\mathbf{g}$	gravity, m/s^2
G_s	solids flux, kg/m^{2}s
m_p	particle mass, kg
P	pressure, Pa
Re	particle Reynolds number
$\mathbf{r}_p$	particle position, m
$\mathbf{S}_p$	momentum source term, N/m^3
t	time, s
$\mathbf{u}_g$	gas velocity, m/s
$\mathbf{U}$	superficial slip velocity, m/s
$\mathbf{v}_p$	particle velocity, m/s
V_{cell}	Eulerian cell volume, m^3
V_b	liquid bridge volume, m^3
x/W	dimensionless riser width

Greek symbols

β	inter-phase momentum transfer coefficient, kg/(m^3 s)
δ_l	liquid layer thickness, m
δ_{pr}	breakage distance of the liquid bridge, m
ϵ_{pr}	height of asperity on the particle surface, m
ε_g	gas volume fraction
γ_l	liquid surface tension, N/m
θ_{nozzle}	main angle of the flat nozzle spray, °
μ	gas viscosity, kg/(m s)
μ_l	liquid viscosity, kg/(m s)
μ_{fr}	dynamic friction coefficient
μ_{nozzle}	mean velocity of droplets leaving the nozzle, m/s
ρ_g	gas density, kg/m^3
ρ_l	liquid density, kg/m^3
ρ_p	particle density, kg/m^3
σ	liquid surface tension, N/m
σ_{nozzle}	standard deviation of droplets velocity leaving the nozzle, m/s
φ	fraction of particle surface covered with liquid
ϕ_s	solids volume fraction
$\boldsymbol{\tau}_g$	stress tensor, Pa

This research focuses on the understanding of the effect of droplets on the hydrodynamics of risers. To determine the relative relevance of the viscous and capillary forces, the capillary number $Ca = \frac{\mu\, v_{rel}}{\gamma_l}$ can be used, where μ is the liquid viscosity, σ the surface tension and v_{rel} the relative velocity between the colliding objects. Low Ca (<0.01) implies negligible contribution of the viscous forces while high Ca (>100) suggests that capillary forces can be dismissed. For intermediate capillary values both forces are relevant and need to be included [20].

To represent those additional forces in a CFD-DEM framework, three main approaches can be found in literature. First of all, the Stokes model [21] is based on an elastohydrodynamic theory and it assumes that the dissipation of the energy is fully dependent on viscous forces. This approach computes a wet/effective restitution coefficient as a function of the dry restitution coefficient and the Stokes number, which describes the interplay of inertia and viscous forces. In this model however, the capillary forces are neglected which results in an over-prediction of the restitution coefficient when it is applied at intermediate capillary numbers [20]. The basis of the second model is to assess the energy balance during the different stages of a wet collision, resulting in algebraic expressions for the wet restitution coefficient. Using this approach, different expressions have been proposed for both the viscous and capillary contributions of the particle–particle and particle–wall collisions [22–24]. Although this approach is computationally efficient as the wet restitution coefficient can be computed at the beginning of the collision, the method is not able to represent agglomerate formation between particles after the collision. The third and final model is able to represent these agglomerates by including the liquid bridges between the particles, which can be done by adding the viscous and capillary forces explicitly in Newton's second law [25,26]. This approach is called the force balance approach. In the wet operation of a riser, the capillary forces are expected to have a significant contribution (see Section 2.4 for more details). Therefore, the Stokes model is rejected. We have chosen to implement the energy balance as it has a lower computational demand compared to the force balance approach. In addition, this method predicts the energy dissipation for small liquid thickness accurately [20], which is a situation that is also expected in the riser.

The main studies on the effect of liquid injection on the hydrodynamics in risers using CFD-DEM are Wang et al. [27] and Girardi et al. [28]. Wang et al. [27] showed the expected increase in flow heterogeneity due to the liquid injection. In addition, the solids distribution is dense at the top and dilute at the bottom of the riser, which is the opposite of the solids distribution in a dry riser. Girardi et al. [28] performed multiple simulations for a small periodic domain that showed a relation between the level of agglomeration and changes in the slip velocities of the particles with the strength of cohesion and liquid loading.

In both these studies, all the particles have initially a uniform wetness, the level of wetness is tuned with the ratio of the liquid volume available for liquid bridges to the particle volume. This results in two arguable assumptions. First, the level of wetness among the particles is homogeneous. However, the large degree of heterogeneity in the solid distribution along the riser and the local injection of the liquid via nozzles will further enhance the heterogeneity of the liquid loading for the particles. Secondly, a particle surface is assumed to be fully covered with liquid, which is only expected when either operating at a low size ratio of the particle compared to the droplet or when particles are hit by a large number of droplets. In all other cases, it is expected that only a fraction of the particle surface is wet leading to only a fraction of collisions having a lower effective, 'wet', restitution.

To include the heterogeneity of the liquid loading among the particles, the liquid droplets are injected as another Lagrangian phase in this research. This approach has been used in DEM simulations of gas–liquid–solid processes such as particle granulation, mixing and coating [22,29–31]. To include the partial liquid coverage of the particle surface, several strategies have been developed to account for the location of the wetted area e.g. spherical harmonics [29], Centroidal Voronoi Tessellation [32] and Fibonacci-Lattice method [30]. However, these solutions lead to additional variables to keep for each particle. Therefore, the surface coverage will be tracked by the surface fraction that is covered with liquid. Particle collisions are treated as wet or dry with a chance related to the surface fraction, which is a trade-off between accuracy and CPU-time. In this work, extreme scenarios will be used to assess the uncertainties of this simplistic approach and the deviation with respect to the assumption of fully covered particles will be determined. As the level of surface coverage depends strongly

on number of droplets that collide with a particle, the simulations considered in this work will be performed with two liquid flow rates, representing high (~29) and typical (~11) particle-to-liquid ratio [33, 34].

This article starts with an introduction of the CFD-DEM model, which focuses on the approaches for the liquid coverage of the particles and collisions between wet particles. In the result section, the differences between the partial coverage and full coverage models are presented. These differences are explained based on the respective wetting properties (coverage fraction and liquid thickness) and their relation with the collisions in the riser.

2. Numerical methods

2.1. Computational fluid dynamics-discrete element method (CFD-DEM)

The CFD-DEM representation is based on the formulations developed for gas–solid systems [35] and specifically the work of Hoomans et al. [36]. The main addition in this work is the droplets as an extra DEM phase. The model considers the gas in the riser as a continuous phase. The volume-averaged Navier–Stokes equations and the continuity equation are used to describe the gas phase hydrodynamics (Eqs. (1) and (2), respectively).

$$\frac{\partial(\varepsilon_g \rho_g \mathbf{u}_g)}{\partial t} + \nabla \cdot (\varepsilon_g \rho_g \mathbf{u}_g \mathbf{u}_g) = -\varepsilon_g \nabla P - \nabla \cdot (\varepsilon_g \boldsymbol{\tau}_g) - \mathbf{S}_u + \varepsilon_g \rho_g \mathbf{g} \tag{1}$$

$$\frac{\partial(\varepsilon_g \rho_g)}{\partial t} + \nabla \cdot (\varepsilon_g \rho_g \mathbf{u}_g) = 0 \tag{2}$$

where $\mathbf{S}_u$ represents the source term due to the momentum transfer between the gas and both particles and droplets:

$$\mathbf{S}_u = \frac{1}{V_{cell}} \sum_{i=1}^{N_p+N_d} \frac{\beta V_a}{1-\varepsilon_g} (\mathbf{u}_g - \mathbf{v}_a) \delta(\mathbf{r} - \mathbf{r}_a) \tag{3}$$

where β is the inter-phase momentum transfer coefficient, computed here with the correlation of Tang et al. [37] for the interaction of the gas with both particles and droplets. The regularized Dirac delta function $\delta(\mathbf{r} - \mathbf{r}_a)$ maps the source term for each of the Lagrangian particles ($a = p$) and droplets ($a = d$) to the relevant Eulerian grid cells. This same delta function maps the gas phase properties and velocities from the Eulerian grid to the particles and droplets position, enabling the evaluation of the drag force. β is the inter-phase momentum transfer coefficient computed with the correlation proposed by Tang et al. [37], which accurately predicts the experimental data of this riser system [38].

The motion of both discrete phases is described using Newton's second law of motion:

$$m_a \frac{d^2 \mathbf{r}_a}{dt^2} = \frac{\beta V_a}{1-\varepsilon_g} (\mathbf{u}_g - \mathbf{v}_a) - V_a \nabla P + m_a \mathbf{g} + \mathbf{F}_{\text{contact},a} \tag{4}$$

The last term of the RHS is only considered for the particles and it accounts for the collisions with other particles and walls. The collisions between particles and droplets require a special treatment, which is explained in Section 2.2. Particle–particle and particle–wall collisions are solved with the soft sphere approach based on a linear spring–dashpot representation proposed by Cundall [39]. However, some of the particles might be (partially) wet due to the interaction with droplets. In these (partially) wet collisions, the capillary and viscous effects should be included, which is explained in detail in Section 2.3. Collisions between droplets are not considered in this work as the droplet-to-particle size ratio is small (<1/15). Also, droplets that hit the walls of the system are immediately removed from the domain.

For the particles, the conservation of angular momentum is also included to obtain the rotational velocities of the particles:

$$\mathbf{I}_a \frac{d\boldsymbol{\omega}_a}{dt} = \mathbf{T}_a \tag{5}$$

Frames from the simulated distribution of solids serve as inputs for a clustering detection model, enabling quantification and characterization of clusters within the riser. Further details on this clustering detection are provided in Ramírez et al. [38].

2.2. Particle–droplet collision

Depending on the physical properties of the particles, the physical properties of the droplets and the conditions at which particle–droplet collisions occur, there are multiple outcomes e.g. partial or total deposition, rebound, complete coating and splashing [40]. In a parametric study, Yoon et al. [40] determined collision outcome maps based on three important variables of particle–droplet collisions, i.e. the Weber number $We = \frac{\rho_d v_{rel}^2 d_d}{\sigma}$, the contact angle and the droplet-to-particle size ratio (DTP). Based on these collision maps [40], the hydrophilic surface of the particles (low contact angle) and the low droplet-to-particle size ratio used in this work (see Section 2.4 for more details) only two possible outcomes are considered: droplet deposition on the particle surface and splashing of the droplets. All collisions with a Weber number below ~170 will result in droplet deposition, while at higher Weber numbers splashing occurs [40]. In the case of deposition, the whole droplet will be added to the liquid volume of a particle, while only 20% of the droplet coats the particle in the splashing regime. The remaining volume forms satellite droplets that are removed from the simulation domain, resembling instant evaporation, similar to Hilton et al. [29]. Although not ideal, the removal of the satellite droplets prevents the increase in computational load for tracking a potentially high number of small droplets. To limit the effect of this approximation, a low Weber number will be promoted with the used conditions (presented in Section 2.4).

To follow the fraction of particle surface covered with liquid, each DEM particle has an additional variable: the coverage fraction (φ). When a droplet deposits on a particle, the change in coverage fraction, $\Delta\varphi$, can be computed by the equilibrium position [41]. When multiple droplets collide with a particle, the contributions of the different droplets should be combined considering especially the possible overlap between the coated patches. This overlap can be considered using two extreme scenarios (schematically shown in Fig. 1) [42]. In the first one, the multiple droplets hit the same spot of the particle (the point-concentrated coverage in Fig. 1), leading to a full overlap between the individual droplet footprints. This scenario, only possible when a stationary non-rotating particle encounter a uniform liquid spray produces the lowest coverage fraction. Therefore, it will be considered the bottom limit of partial coverage in this research. The total coverage fraction can be easily calculated from the equilibrium position of the single droplet that is formed.

In the second approach (the uniformly-random coverage in Fig. 1), the particle's displacement and rotation relative to the liquid spray are so high that droplets can hit any part of the particle, which decreases the overlap of the droplets compared to the first approach. However, the chance of hitting a dry part of the particle decreases with previous depositions of previous droplets. With this approach the total coverage fraction will serve as the upper limit of partial coverage. Its implementation in this research is based on the work of Kariuki et al. [43], with a slight modification to handle droplets with different sizes (see Eq. (6)).

$$\varphi = 1 - \left[\prod_{i=1}^{N_{coll}} (1 - \Delta\varphi_i) \right] \tag{6}$$

Fig. 2 presents a comparison of the evolution of the coverage fraction for one particle as function of the number of hitting droplets for the partial coverage approaches. The droplet-to-particle size ratio and contact angle used in this comparison are representative of the simulation settings of this study. It is clear that the uniformly-random approach is already covered fully while only 38% coverage is obtained with the point-concentrated coverage.

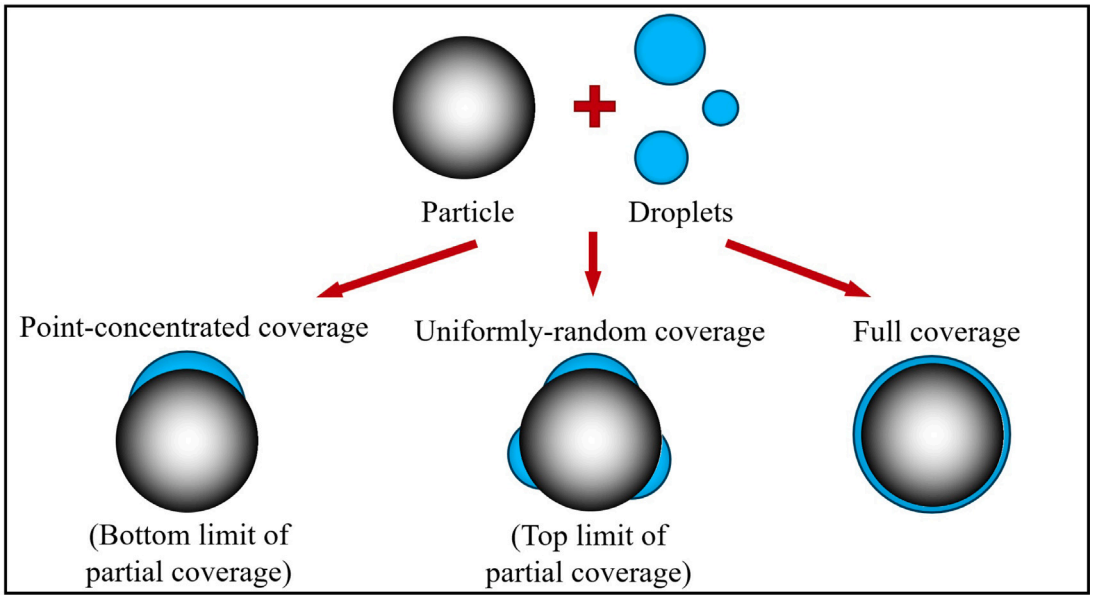

Fig. 1. The liquid coverage approaches considered in this work.

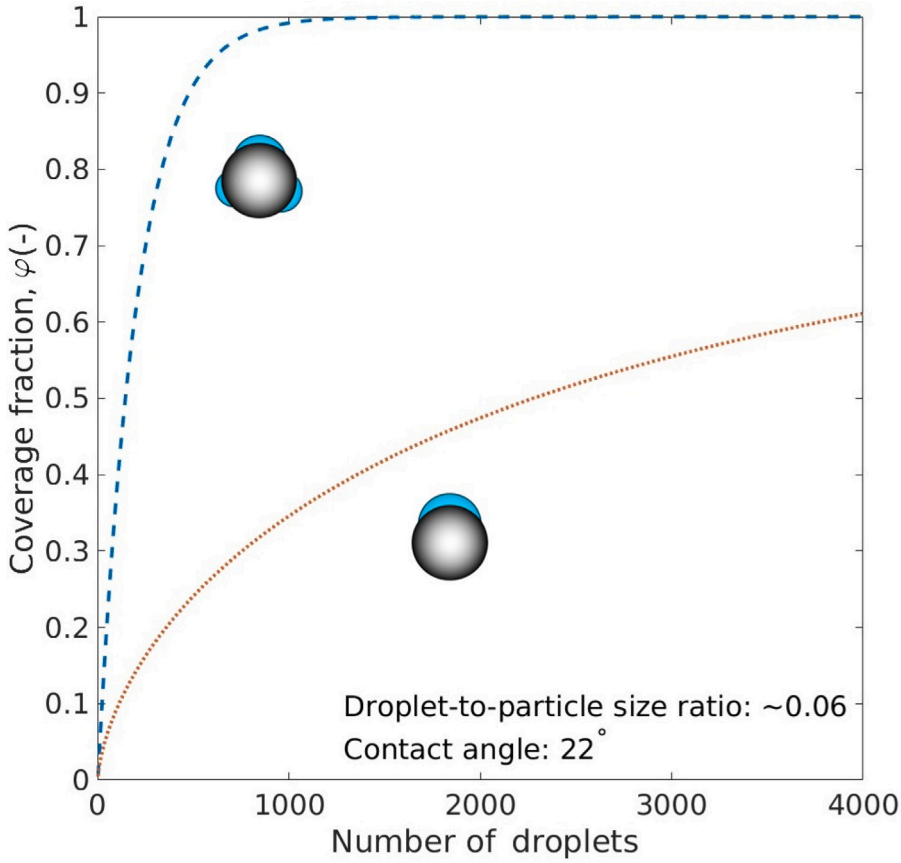

Fig. 2. Coverage fraction, φ, as a function of the number of droplets. The comparison of the point-concentrated and uniformly-random coverage approaches.

In addition to the coverage, the liquid thickness on the surface is important. For the point-concentrated coverage, the thickness can be directly computed with Eq. (7) when the coverage fraction is known. This determination is not trivial for the uniformly-random coverage as the surface of the particle might have high spatial variability of the thickness as a result of a non-uniform wetting [42]. To reduce the computational expenses, the liquid layer is assumed to be uniform for a particle and is calculated using the liquid coverage and Eq. (7). Besides the two partial coverage approaches, the full coverage assumption with a uniform liquid layer thickness will be also evaluated. In this case, φ is equal to 1 regardless of the number and size of the hitting droplets and the thickness is also obtained with Eq. (7).

Table 1
Summary of the approaches to compute the energy dissipated (ΔE) for wet collisions. Stages of collision, I: approaching through liquid layer, II: solid–solid contact, III: separation and liquid bridge rupture. v_i refers to the velocity after the stage of collision i. In the table, four different types of energy dissipation mechanisms are considered: viscous forces (*vis*), liquid acceleration (*acc*), capillary forces (*cap*) and contact (*con*).

Stage	Particle–wall collision (Sutkar et al. [22]	Particle–particle collision (Shabanian et al. [24]
I	$\Delta E_{vis} = \frac{3}{8}\mu_l d_p^2 v_0 \ln(\frac{\delta_l}{\epsilon_{pr}}) - \frac{9}{128}\frac{\pi^2\mu_l^2 d_p^4}{m_p}$ $\Delta E_{acc} = \frac{1}{2}\rho_l \pi d_p^3 \left(\frac{\delta_l}{d_p}\right)^2 \times \left(\frac{1}{2} - \frac{\delta_l}{3d_p}\right) v_0^2 \left(\frac{d_p}{\delta_l} - 1\right)$	$\Delta E_{vis} = \frac{3}{8}\mu_l d_p^2 v_0 \ln(\frac{f(\delta_l)}{f(\epsilon_{pr})}) + \frac{9}{128}\frac{\pi^2\mu_l^2 d_p^4}{m_p}(\ln^2(f(\delta_l)) - \ln^2(f(\epsilon_{pr})) - 2\ln(f(\delta_l))\ln(\frac{f(\delta_l)}{f(\epsilon_{pr})}))$ $\Delta E_{cap} = -\pi\gamma d_p \cos\theta((\delta_l - \sqrt{\delta_l^2 + a^2}) - (\epsilon_{pr} - \sqrt{\epsilon_{pr}^2 + a^2}))$
II	$\Delta E_{con} = \frac{1}{2} m_i \left(1 - e_n^2\right) v_I^2$	$\Delta E_{con} = \frac{1}{2}\frac{m_i m_j}{m_i + m_j}\left(1 - e_n^2\right) v_I^2$
III	$\Delta E_{vis} = \frac{3}{8}\mu_l d_p^2 v_{II} \times \left(\ln(\frac{\delta_l}{\epsilon_{pr}}) - ln(\frac{\delta_{pr}}{\epsilon_{pr}})\right)$ $\Delta E_{acc} = \frac{1}{2}\rho_l \pi d_p^3 \left(\frac{\delta_l}{d_p}\right)^2 \times \left(\frac{1}{2} - \frac{\delta_l}{3d_p}\right) v_{II}^2 \left(\frac{d_p}{\delta_l} - 1\right)$ $\Delta E_{cap} = \pi\gamma\sqrt{2V_b d_p}$	$\Delta E_{vis} = \frac{3}{8}\mu_l d_p^2 v_{II} \ln(\frac{f(\delta_{pr})}{f(\epsilon_{pr})}) - \frac{9}{128}\frac{\pi^2\mu_l^2 d_p^4}{m_p}(\ln^2(f(\delta_{rp})) - \ln^2(f\epsilon_{pr})) - 2\ln(f(\delta_{pr}))\ln(\frac{f(\delta_{pr})}{f(\epsilon_{pr})})$ $\Delta E_{cap} = \pi\gamma d_p \cos\theta(\left(\delta_{pr} - \sqrt{\delta_{pr}^2 + a^2}\right) - \left(\epsilon_{pr} - \sqrt{\epsilon_{pr}^2 + a^2}\right))$
	with: $V_b = \frac{d_p^3}{16}$	with: $H(r) = 2D + \frac{2r^2}{d_p}$ $V_b = \frac{1}{4}\pi d_p(H^2(r_w) - 4\epsilon_{pr}^2) \quad a^2 = \frac{V_b}{\pi d_p}$ $f(x) = \frac{x\sqrt{x^2+a^2}}{(x+\sqrt{x^2+a^2})^2}$

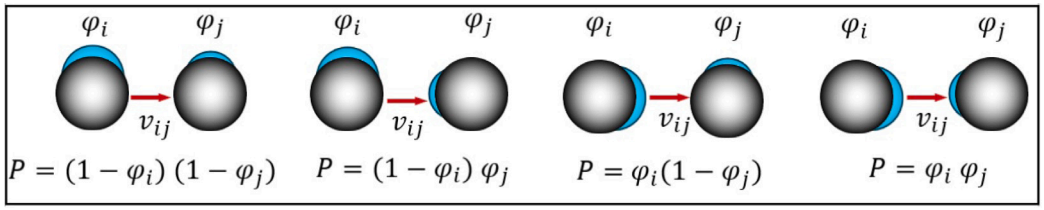

Fig. 3. The possible interactions of two partial wet particles with their probability, P.

$$\delta_l = \sqrt[3]{\frac{3V_{dep}}{2\pi(1-\cos\theta_w)} + R_p^3} - R_p \qquad \text{with} \quad \cos\theta_w = 1 - 2\varphi \tag{7}$$

Finally, the particle velocity will change due to the particle–droplet collision. This change in velocity can be obtained using the momentum conservation equation (Eq. (8)). Note that f_{dep} accounts for the fraction of the droplet deposited on the particle surface. Furthermore, it is assumed that the angular velocity is unaffected by the particle–droplet collision.

$$\mathbf{v}_p' = \frac{m_p\mathbf{v_p} + f_{dep}m_d\mathbf{v_d}}{m_p + f_{dep}m_d} \tag{8}$$

2.3. Wet particle collision

When partial coverage is considered, different collisions are possible based on the nature of the surfaces that are in contact; the collision can occur between dry–dry, dry–wet or wet–wet surfaces. This is illustrated in Fig. 3 for two particles with coverage fractions of φ_i and φ_j with their probability P.

A collision with wet particles results in additional contributions from the viscous and capillary forces. Before the particles are in contact, the objects have to penetrate the liquid film between them resulting in a resistance. Similarly, this liquid film will impose a resistance during the separation of the objects after the collision. Additionally, the formation and rupture of a liquid bridge between the particles contribute to the energy dissipation. In our modeling approach, each one of these additional steps have an associated expression to compute the energy dissipated. As some of these expressions are semi-empirical formulations, the studies of Sutkar et al. [22] and Shabanian et al. [24] were followed for particle–wall and particle–particle collision, respectively. Table 1 shows the used equations for both type of collisions. These two studies also differ in the way to combine those individual energy dissipation to predict the outcome of the collision. In Sutkar et al. [22], a restitution coefficient for each stage of the collisions can be obtained with the expressions in Table 1, and the global restitution coefficient for the collision is the product of the individual restitution coefficients. While in Shabanian et al. [24], the energy dissipation is calculated differently as the dissipated energy is removed from the initial kinetic energy of the particle for each stage of the collision sequentially. Note that, the model of Sutkar et al. [22] has a contribution due to the energy required for the acceleration of the liquid film during the approach of the particles and the separation. This energy contribution is not included in the model of Shabanian et al. [24] where only viscous and capillary effects are considered in the approaching and separation steps.

2.4. Simulation conditions

A schematic representation of the simulated riser is shown in Fig. 4 and the settings are given in Table 2. A detailed description for the dry operation is given in Varas et al. [44]. Dry particles are injected from the downcomer Ⓑ via a dosage slit located 40 mm above the bottom of the riser. This feeding channel is inclined at an angle of 45° and its feeding rate ensures a solids flux of ~32 kg/m^{2}s. The particles travel along the riser by the dry air injected from the bottom. The liquid droplets are injected by the nozzle Ⓖ located 100 mm above the bottom of the riser with an inclination of 15°.

The velocity of the injected particles was set to $\{0.2, 0.0, -0.2\}$ m/s. The particles are injected at a random position along 20 mm next to the left wall and 40 mm above the bottom of the riser. In case of overlap of an injected particle with a particle in the domain, the model will try new locations, if there is no position without overlap in 100 trails the simulation proceeds without particle injection until the next time step.

At the elbow at the top, the non-slip boundary condition was imposed using an Immersed Boundary Method [45]. The top, front, back and right walls have a non-slip boundary condition. The left wall in Fig. 4 contains an outflow boundary condition for the final 7 cm, here the pressure is set to 1 atm. At the bottom of the domain, the gas velocity is set with $U_{g,in}$ = 6.35 m/s. With this gas velocity the riser is operated in the fast fluidization regime. The grid resolution was

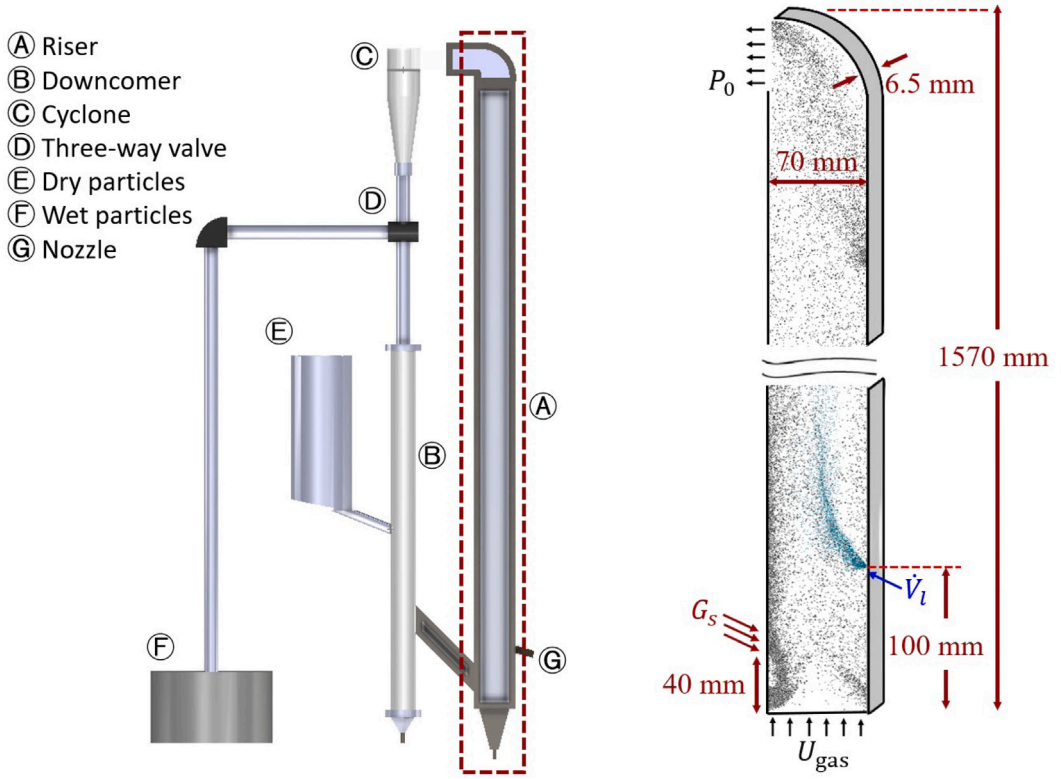

Fig. 4. A schematic representation of the considered riser.

similar to Varas et al. [8], which showed it was sufficient to capture the hydrodynamic behavior. Table 2 shows different time steps for the continuous and discrete phases. While Δt_{flow} is small enough to guarantee that the Courant number is below 0.1, a smaller Δt_{DEM} is required for a good representation of the particle dynamics, particularly the contact force. The choice of Δt_{DEM} is typically taken as 1/10 of the duration of a collision, which for a linear spring–dashpot model is governed by the ratio of the effective mass of the collision and the chosen spring stiffness [46].

Given the pseudo-2D nature of the riser, this research represents the liquid injection with a flat fan nozzle, where the planar shape of the spray can be defined with the combination of a major (θ_{nozzle}) and a minor (γ_{nozzle}) angle. Table 3 presents information of two nozzles which have a comparable liquid velocity and droplet size distribution, but different flow rate. These flow rates correspond respectively to high (~29.1) and typical (~11.2) particle-to-liquid volume ratio. Higher liquid flow rates may cause excessive droplet deposition on the walls of the pseudo-2D riser, which the model at the moment cannot reproduce.

At the start of each simulation, the riser is filled with dry particles which reaches a pseudo-state condition. Subsequently, droplets are injected and the simulations are continued for 5 s to obtain the new pseudo-steady state. The results presented in this work are obtained by averaging over 10 s in this new pseudo-steady state. The flow fields and void fraction profiles are obtained every 0.05 s. In addition, the particle clusters are obtained from each void fraction field using a core-wake approach based on constant thresholds, which is explained in detail in Ramírez et al. [38].

The CFD-DEM model used in this work is in the in-house code Foxberry [47]. All simulations are performed on a single thread of an AMD Ryzen Threadripper 2950X processing unit. The simulation time for a simulation of 1 s with 30000 particles is one day. In the current simulations, the number of particles depends largely on the liquid flow rate and the liquid coverage approach and ranges between 40000 and 80000.

Table 2
The simulation settings.

L (m)	0.07	d_p = (mm)	0.85
H (m)	0.0065	Δt_{flow}(s)	5×10^{-5}
D (m)	1.57	Δt_{DEM}(s)	5×10^{-6}
Δx (m)	2.5×10^{-3}	k_n(N/m)	1587
Δy (m)	1.25×10^{-3}	$e_{n_{p-p}}$	0.96
Δz (m)	2.5×10^{-3}	$e_{n_{p-w}}$	0.86
G_s (kg/m^{2}s)	32.0	$\mu_{fr_{p-p}} = \mu_{fr_{p-w}}$	0.15
$U_{g,in}$ (m/s)	6.35	$e_{t_{p-p}} = e_{t_{p-w}}$	0.33
ρ_p (kg/m^3)	2500		

3. Results

3.1. Effect of the liquid coverage approach

Fig. 5 presents the time-averaged comparison of a dry riser and the three different coating approaches for the low liquid flow (0.03 l/min). In Fig. 5a, the contours of the solids fraction show that all three coverage approaches have a higher solids content compared to the dry case. In addition, the solids content seems to increase with an increase of the coverage of the particles. Fig. 5b shows the time- and laterally-averaged axial profiles. All cases show a higher solids density at the bottom that sharply decreases along the riser as expected for the fast fluidization regime. Contrary to Fig. 5a, there is no clear difference between the axial profiles of the dry case and the two partial coverage approaches. Only the full coverage approach has a significant increase in the solids holdup. This could be explained by the coverage fraction being significantly lower than 1 for both partial coverage approaches. It is expected that an increase in the liquid flow rate is required to obtain significant changes from the dry profile.

Table 3
Nozzle settings.

		Nozzle 1	Nozzle 2
Flow (l/min)		0.03	0.078
Normal velocity distribution	μ_{nozzle}(m/s)	9.87	11.80
	σ_{nozzle}(m/s)	3.00	3.68
Weibull radius distribution	shape parameter, a	1.41	1.28
	scale parameter, b	2.20×10^{-5}	2.08×10^{-5}
θ_{nozzle}(°)		16.2	27.9
γ_{nozzle}(°)		5.1	10.5

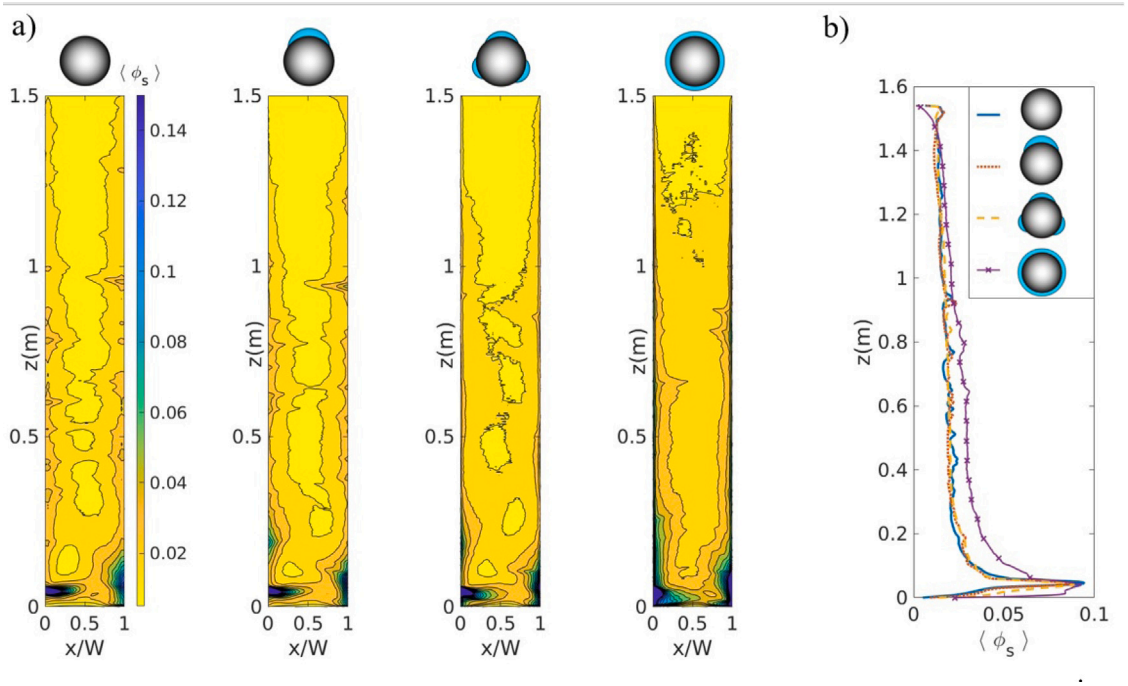

Fig. 5. The time-averaged results for a riser in dry operation and wet operation with $\dot{V}_l = 0.03$ l/min using the point-concentrated, uniformly-random and full coverage approaches. The figure shows a) the contour of solids volume fraction and b) the axial profiles of laterally-averaged solids holdup.

3.2. Effect of liquid flow rate

3.2.1. Solids volume fraction and solids flux

Fig. 6 shows the number of particles in the riser for both liquid flow rates. First of all, Fig. 6a shows a good correspondence with the results in Fig. 5. Although both partial coverage approaches present a slight increase in the number of particles compared to the dry case, the full coverage has a significant increase in the number of particles inside the riser. When a liquid higher flow rate is applied (Fig. 6b), the difference between the dry case and both partial coverage approaches is more evident. Besides, the increase for the uniformly-random partial coverage model is larger than the point-concentrated approach. It is expected that this is caused by the increased liquid coverage in the case of the uniformly-random approach, which is closer to the full coating approach.

Fig. 7 shows the radial profiles of the time-averaged solids holdup for the bottom section (first row) and top section (second row) of the riser, for both liquid flow rates. Regardless of the liquid flow rate, the profiles in the top section are more flat compared to the profiles in the bottom, which is a consequence of the higher solids density in the bottom. In addition, the solids content in the full coverage approach is higher for all cases, confirming the higher solids holdup discussed above. The two partial coverage approaches and the dry model show very similar results at low liquid flow rates. At the higher liquid flow rate and specifically at the bottom section, both partial coverage approaches are comparable to those found with the full coverage approach. However, the results with the point-concentrated approach seem to flatten while the results with uniformly-random approach retain a radial gradient similar to the full coverage approach. Finally, the increase of the liquid flow rate does not have a major influence on the predictions of the full coverage approach. Therefore, the liquid thickness does not influence the solids volume fraction, which would be expected as an increase in the liquid layer would lead to an increase in the dissipation of energy. This could suggest that most of the wet collisions have reached a point where all momentum is dissipated. This point is addressed further in Section 3.3.

The time-averaged solids flux profiles are presented in Fig. 8. The solids fluxes in Fig. 8 show the same trends as the solids holdup profiles. The figure clearly shows that the increase in the liquid flow rate increases the radial variation in the predictions of the partial coverage approaches especially for the uniformly-random coating. Another similarity is the small effect of the different liquid flow rates for the results with the full coverage approach. This result suggests that there is more solids circulation, leading to potentially more and or larger clusters in the system. In terms of numerical performance, comparing the dry case to the liquid coverage approaches for the higher liquid flow rate, the cpu-time of the full coverage approach is around 44% higher than the dry case, which is caused by the new DEM droplets in the system and the computation of particle–droplet collisions. An additional 13% increase in cpu-time is encountered when any of the two partial coverage approaches is implemented.

3.2.2. Clustering behavior

Fig. 9 presents the cluster frequency (defined as cluster per frame) as a function of the non-dimensional width of the bed. All models show the

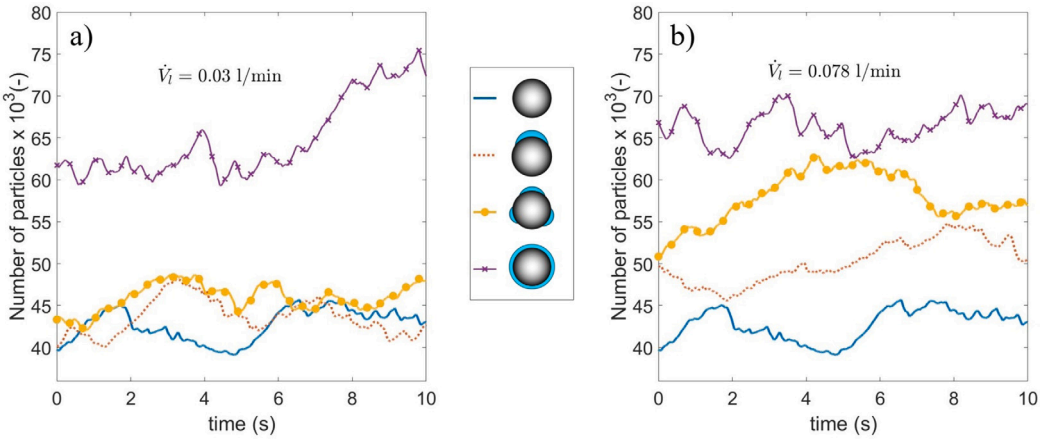

Fig. 6. The number of particles inside the riser in pseudo steady state as a function of time. The results are presented for the dry riser and the wet riser with the three different liquid coverage approaches. (a) $\dot{V}_l = 0.03$ l/min, (b) $\dot{V}_l = 0.078$ l/min.

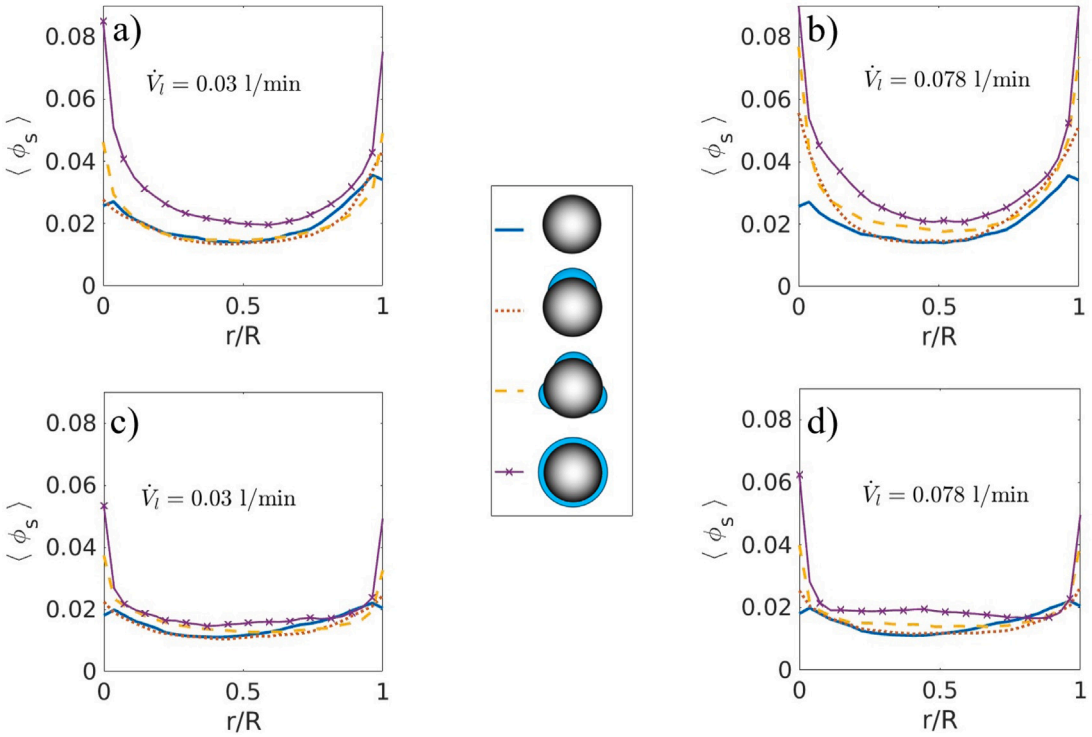

Fig. 7. The radial profiles of the time-averaged solids holdup for two liquid flow rates. The profiles in bottom section of the riser (z = 0.5 m) are shown in figures a and b for $\dot{V}_l = 0.03$ and 0.078 l/min, respectively. The second row shows the profiles at the top section of the riser (z = 1.1 m) in figure c and d for $\dot{V}_l = 0.03$, 0.078 l/min, respectively.

expected preference for the formation of clusters near the walls, which can also be expected based on the core-annulus structure presented in Fig. 7. For the lower liquid flow rate (Fig. 9a), the clustering behavior is changed for both partial coverage approaches compared to the dry riser, i.e. more clusters are obtained near the wall. The differences between the dry case and the full coverage approach are even more significant. Increasing the liquid flow rate (Fig. 9b) has the largest effect on the uniformly-random approach, which is also shown in the solids holdup and flux.

Fig. 10 shows an analysis of the cluster area. At the low liquid flow rate, the partial coverage approaches predict a cluster area similar to the cluster area predicted in the dry case, while the difference is more pronounced at the high flow rate. On the contrary, the full coverage approach shows a significant increase in the cluster area even with the low liquid flow rate, while the increase in liquid flow rate has a minor effect on the cluster area. This suggests a small effect of the liquid layer thickness and a large effect of the coverage fraction.

3.3. Particle wetness characterization and relation with energy dissipation

Fig. 11 presents the coverage fraction probability distribution for the partial coverage approaches as a function of the liquid flow rate. As expected, the distribution with the point-concentrated coverage results in a lower coverage fraction compared to the uniformly-random approach for all the liquid flow rates. Comparing the two approaches, it is also noticeable that an increase in the liquid flow rate has a more significant impact for the uniformly-random approach, which is expected based on the behavior reported in Fig. 2. It could also explain the differences observed in Section 3.2 for the low and high liquid flow rates.

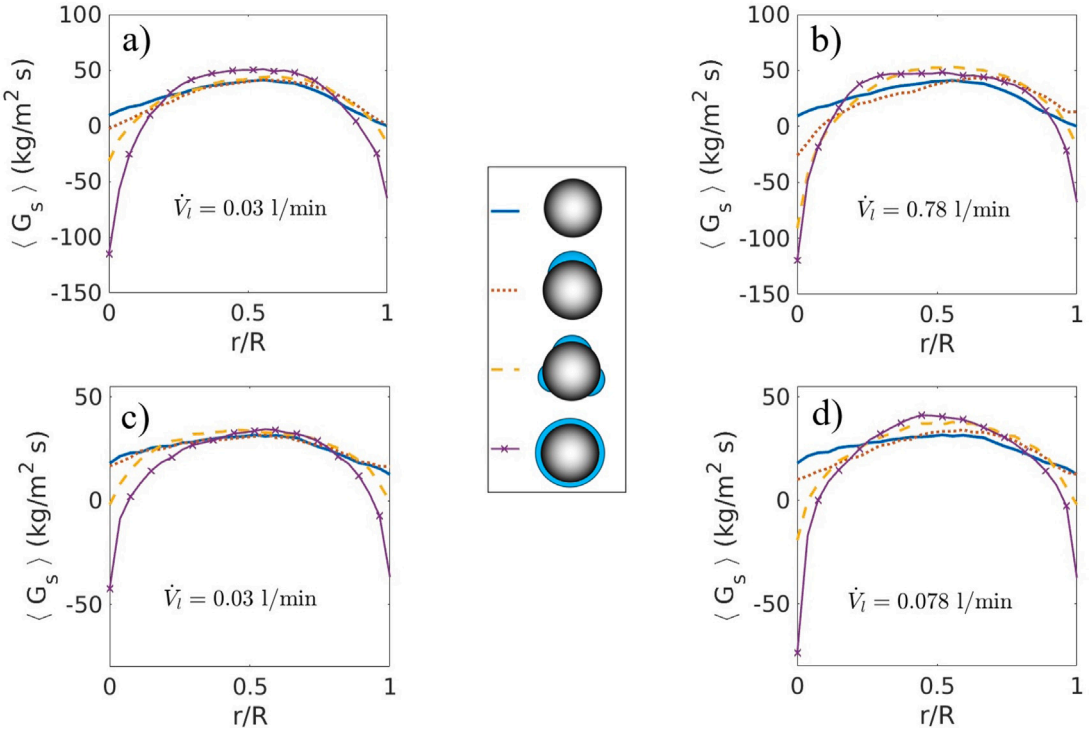

Fig. 8. The radial profiles of time-averaged solids flux for both liquid flow rates. The profiles in bottom section of the riser (z = 0.5 m) are shown in figures a and b for $\dot{V}_l$ = 0.03 and 0.078 l/min, respectively. The second row shows the profiles at the top section of the riser (z = 1.1 m) in figure c and d for $\dot{V}_l$ = 0.03 and 0.078 l/min, respectively.

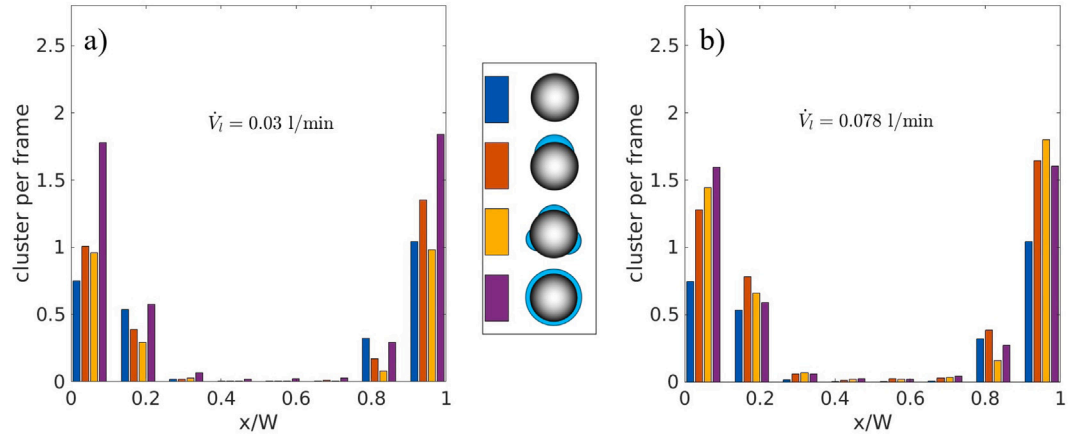

Fig. 9. The cluster frequency for both liquid flow rate. The results are presented for the dry case and the point-concentrated, uniformly-random and full coverage approaches.

Based on the two extreme models with respect to the coverage fraction, the full coverage approach deviates significantly from the two partial approaches. However, the distribution obtained with the uniformly-random approach converges to the full coating assumption when high liquid flow rates are used. Finally, it is important to mention that regardless of the liquid flow rate a considerable part of the particles is not wet for the partial coverage approaches, which is indicated by the zero coverage in Fig. 11.

Details on the percentage of wet particles are presented in Table 4. It is remarkable that according to Table 4 the percentage of wet particles is >85% for low liquid flow rates independent of the coverage approach. In addition, the percentage of wet particles is increased when the liquid flow rate is increased. The table also shows that the liquid thickness is decreasing from the point-concentrated approach to the full coverage approach, as is expected with an increase in the coverage fraction and a similar global liquid loading. This suggest that all the features studied in the previous sections can be attributed to the chance of having a wet collision and or the amount of dissipated energy per collision, related to the film thickness.

Fig. 12 presents the probability density function of the wet restitution coefficient for the three coating approaches. There is a high probability to compute a collision with a low restitution coefficient regardless of the liquid flow rate, especially for the full coverage approach. The uniformly-random approach predicts a restitution coefficient of approximately zero for >65% of the collisions. There is a relation between the wetness characteristics discussed above and the behavior in Fig. 12. As expected, the highest restitution coefficient is more prominent in the point-concentrated approach as the chance of dry–dry collision is the highest in this model, while the chance of high restitution coefficient is the lowest in the full coverage approach. However, the absence of intermediate restitution coefficients is remarkable, i.e. all combinations of wet collisions are captured in the lowest restitution coefficient. To understand this phenomenon, Fig. 13a presents the cumulative distribution of the relative velocity before

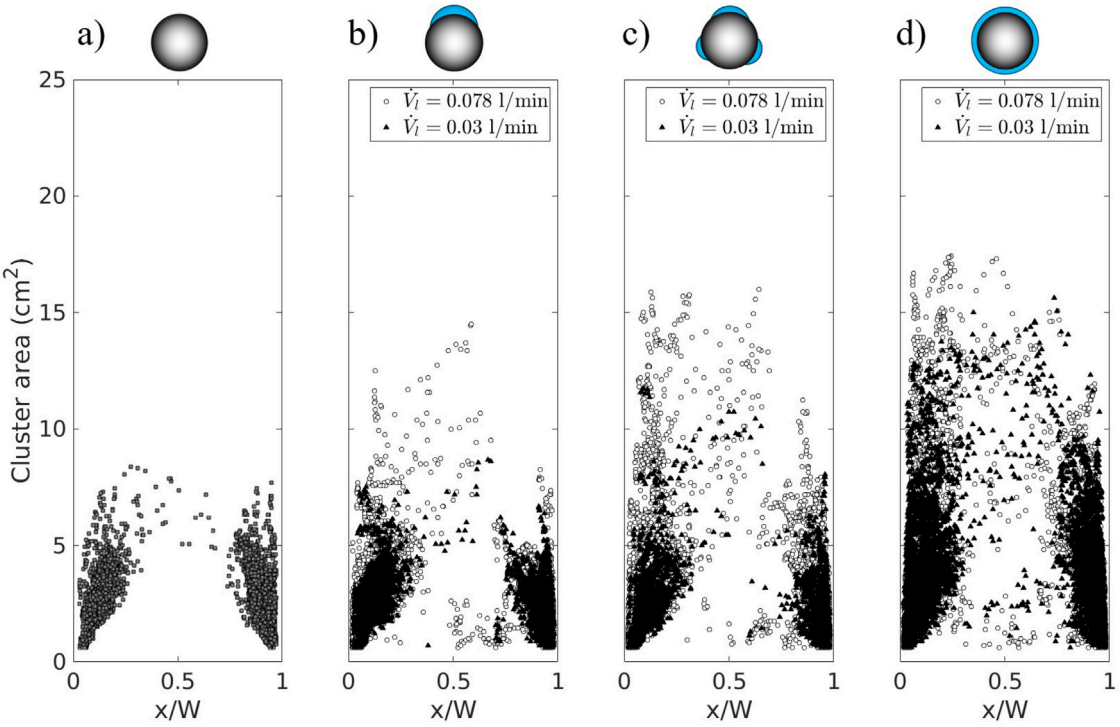

Fig. 10. The cluster area vs centroid of the clusters for the dry operation and the wet operation with both liquid flow rates and the different coating approaches.

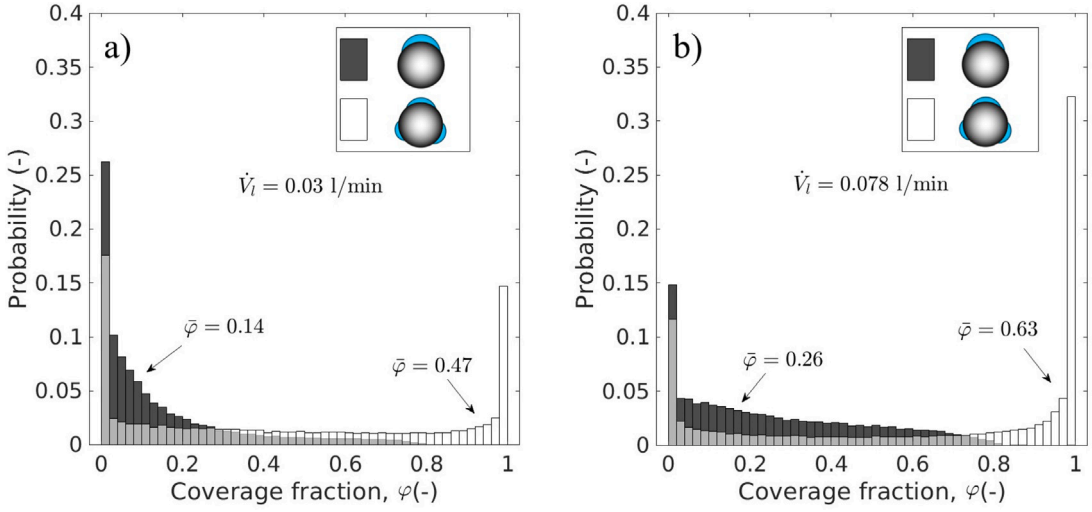

Fig. 11. Coverage fraction probability distribution. (a) $\dot{V}_l = 0.03$, (b) $\dot{V}_l = 0.078$l/min.

Table 4
The percentage of wet particles inside the riser and the average liquid thickness as a function of the liquid flow rate and the liquid coverage approach (between brackets in μm).

Liquid flow rate (l/min)	Liquid coverage approach		
	Point-concentrated	Uniformly-random	Full coverage
0.03	86.3% (42.8)	85.5% (23.7)	88.3% (18.5)
0.078	90.2% (70.2)	90.8% (38.9)	95.1% (33.4)

particle–particle collisions for the full coverage approach with the low liquid flow rate. 50% and 90% of the collisions have a relative particle velocity below 0.0022 m/s and 0.1 m/s, respectively. Fig. 13b presents the restitution coefficient predicted for collisions occurring for 0.0022 m/s and 0.1 m/s as a function of the liquid thickness. According to the graph, a collision occurring at 0.0022 m/s will result in a restitution coefficient equal to zero for virtually any liquid thickness, while at a relative velocity of 0.1 m/s also intermediate restitution coefficients are predicted. However, the restitution coefficient is zero even with liquid layer thickness below the average (19 μm). Based on this analysis, Fig. 12a is not unreasonable. In addition, it would also explain the small dependency on the liquid flow rate for the full coverage approach. Similarly, it explains why the increase in coverage fraction observed for the partial coverage approaches produced a clear different behavior

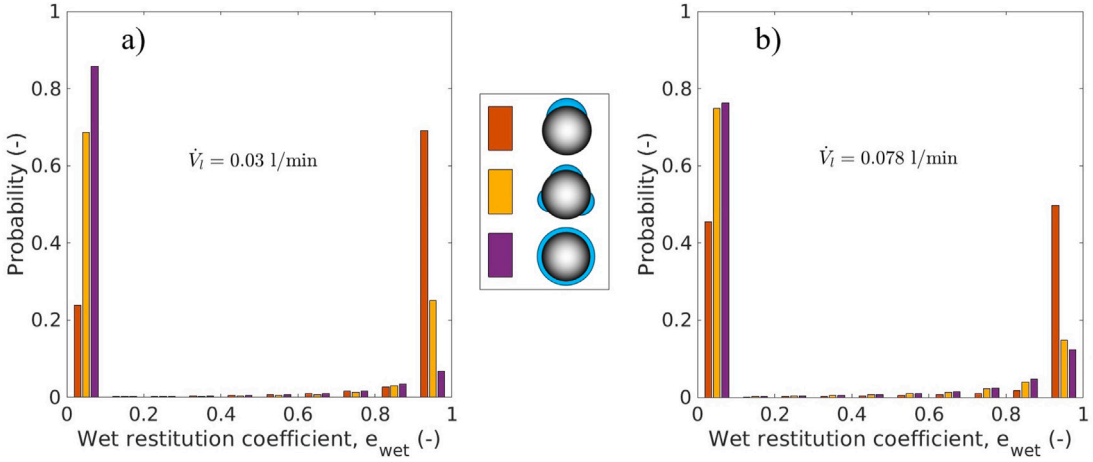

Fig. 12. Probability distribution function of wet restitution coefficient. (a) $\dot{V}_l = 0.03$, (b) $\dot{V}_l = 0.078$l/min. Results are presented for the point-concentrated, uniformly-random and full coverage approaches.

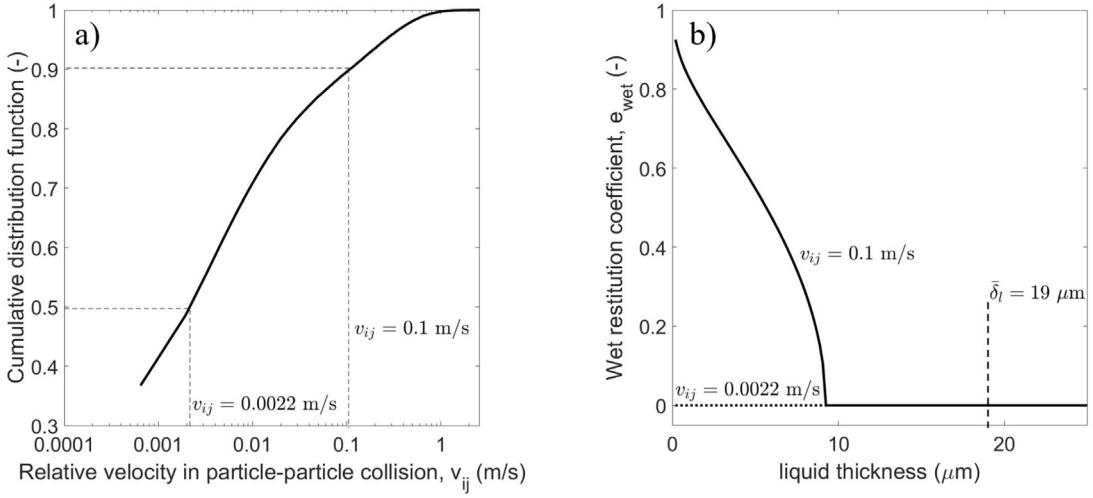

Fig. 13. Behavior of collision variables using the full coverage approach and $\dot{V}_l = 0.03$l/min. (a) cumulative distribution function of the relative velocity in particle–particle collision. (b) behavior of wet restitution coefficient as a function of the liquid thickness for different relative collision velocities.

inside the riser. Further numerical and experimental research must be conducted as such a large amount of collisions with a low restitution might indicate the formation of particle agglomerates that persist with time. A level of confirmation is found in the CFD-DEM results of Girardi et al. [28], that for similar conditions of solids fraction and balance between the attractive force due to the liquid and particle weight, their simulation presented the same strong agglomeration even with liquid loads ten times smaller than the ones used in this study. This agglomerate formation is not captured by the energy balance approach described here.

4. Conclusions

A hydrodynamic evaluation of a riser in the fast fluidization regime with liquid injection was carried out using CFD-DEM. In our approach, particles and droplets were simulated as Lagrangian objects. This approach showed an uneven liquid loading among the particles and an uneven distribution of the liquid over the particle surface. Our study confronted the ideal scenario of a fully covered particle with two approaches of partial coating of the particle surface. These two partial coverage approaches differ in the way they handle multiple droplets colliding with the same particle. These two approaches are the expected lower (point-concentrated approach) and upper (uniformly-random approach) bounds of the coverage fraction. Our study used two different liquid flow rates corresponding to a low and a typical amount of liquid injection with respect to the particles. The comparison of the liquid coverage approaches showed a high dependence on the liquid flow rate.

At low liquid flow rate, the partial coverage approaches predicted 14% and 47% coverage of the particle surface with droplets, which is considerably lower than the assumption of full coverage. In correspondence, the behavior of the riser in terms of solids holdup and cluster formation for the partial coverage approaches was more similar to the behavior of the dry riser than the behavior with fully covered particles.

At higher liquid flow rate, the uniformly-distributed random approach reached an average of 63% particle coverage and more than one third of the particles showed full coverage. Therefore, the predictions are similar to those obtained with the full coverage assumption. The point-concentrated coverage approach predicted an average of 26% coverage of the particle, leading to a noticeable increase of the clusters size but only a minor change in terms of cluster frequency and the solids holdup profiles.

The increase in liquid flow rate had a negligible influence on the predictions of the full coverage approach suggesting that the changes in the coverage fraction are more relevant than changes in the liquid thickness for our system. This was confirmed by analyzing the probability distribution of the restitution coefficient for the different simulation cases. These showed that the restitution coefficient is either close to the

dry value (in case of dry–dry surfaces in contacts) or close to zero for almost all possible combinations of wet collisions. This is due to the low relative velocities between the colliding particles.

Despite the good assessment of particle wetness (coverage fraction and thickness) obtained with two extreme cases of partial coverage and the impact on risers hydrodynamics demonstrated, an experimental validation should be conducted especially for the high number of collisions predicted with very low restitution coefficients. This might suggest that particles will form persistent agglomerates, which is a phenomenon that cannot be captured with the implemented energy balance approach. Further research must be conducted on how to select the most appropriate liquid coverage model based on actual operational conditions such as particle-to-liquid ratio, linear and angular velocity of the particles and spray shape. Future numerical developments should also incorporate heat and mass transfer between the three phases, as evaporation, for example, could reduce the impact of liquid injection on the hydrodynamics discussed here.

CRediT authorship contribution statement

Juan G. Ramírez: Writing – original draft, Visualization, Validation, Software, Methodology, Investigation, Formal analysis, Data curation, Conceptualization. **Levi Peene:** Investigation, Formal analysis, Data curation. **Maike Baltussen:** Writing – review & editing, Supervision, Software, Methodology, Investigation, Funding acquisition, Formal analysis. **Kay Buist:** Writing – review & editing, Supervision, Investigation, Funding acquisition, Formal analysis. **Johannes A.M. (Hans) Kuipers:** Writing – review & editing, Supervision, Software, Project administration, Methodology, Funding acquisition, Formal analysis, Conceptualization.

Declaration of competing interest

The authors declare the following financial interests/personal relationships which may be considered as potential competing interests: J.A.M. Kuipers reports financial support was provided by Netherlands Center for Multiscale Catalytic Energy Conversion (MCEC). If there are other authors, they declare that they have no known competing financial interests or personal relationships that could have appeared to influence the work reported in this paper.

Acknowledgment

This work was supported by the Netherlands Center for Multiscale Catalytic Energy Conversion (MCEC), an NWO Gravitation programme funded by the Ministry of Education, Culture and Science of the government of the Netherlands.

Data availability

Data will be made available on request.

References

[1] M.T. Shah, R.P. Utikar, V.K. Pareek, G.M. Evans, J.B. Joshi, Computational fluid dynamic modelling of FCC riser: A review, Chem. Eng. Res. Des. 111 (2016) 403–448.
[2] X. Jian-jun, Y. Xue-min, Z. Lei, D. Tong-li, S. Wen-li, L. Wei-gang, Emissions of SO2, NO and N2O in a circulating fluidized bed combustor during co-firing coal and biomass, J. Environ. Sci. 19 (1) (2007) 109–116.
[3] F. Berruti, T.S. Pugsley, L. Godfroy, J. Chaouki, G.S. Patience, Hydrodynamics of circulating fluidized bed risers: A review, Can. J. Chem. Eng. 73 (5) (1995) 579–602.
[4] E. Helland, H. Bournot, R. Occelli, L. Tadrist, Drag reduction and cluster formation in a circulating fluidised bed, Chem. Eng. Sci. 62 (2007) 148–158.
[5] G.J. Heynderickx, A.K. Das, J.D. Wilde, G.B. Marin, Effect of clustering on gas-solid drag in dilute two-phase flow, Ind. Eng. Chem. 43 (2004) 4635–4646.
[6] J. Xu, J.X. Zhu, Visualization of particle aggregation and effects of particle properties on cluster characteristics in a CFB riser, Chem. Eng. J. 168 (2011) 376–389.
[7] X. Lan, X. Shi, Y. Zhang, Y. Wang, C. Xu, J. Gao, Solids back-mixing behavior and effect of the mesoscale structure in CFB risers, Ind. Eng. Chem. 52 (2013) 11888–11896.
[8] A.E.C. Varas, E.A.J.F. Peters, J.A.M. Kuipers, CFD-DEM simulations and experimental validation of clustering phenomena and riser hydrodynamics, Chem. Eng. Sci. 169 (2017) 246–258.
[9] L. Mu, K.A. Buist, J.A.M. Kuipers, N.G. Deen, Scaling method of CFD-DEM simulations for gas-solid flows in risers, Chem. Eng. Sci.: X 6 (2020).
[10] T. Tanaka, S. Yonemura, K. Kiribayashi, Y. Tsuji, Cluster formation and particle-induced instability in gas-solid flows predicted by the DSMC method, JSME Int. J. Ser. B 39 (1996) 239–245.
[11] T. Wang, Y. He, S. Yan, T. Tang, H.I. Schlaberg, Cluster granular temperature and rotational characteristic analysis of a binary mixture of particles in a gas-solid riser by mutative smagorinsky constant SGS model, Powder Technol. 286 (2015) 73–83.
[12] M.T. Shah, R.P. Utikar, M.O. Tade, V.K. Pareek, Hydrodynamics of an FCC riser using energy minimization multiscale drag model, Chem. Eng. J. 168 (2011) 812–821.
[13] N. Yang, W. Wang, W. Ge, J. Li, CFD simulation of concurrent-up gas-solid flow in circulating fluidized beds with structure-dependent drag coefficient, Chem. Eng. J. 96 (2003) 71–80.
[14] K.N. Theologos, A.I. Lygeros, N.C. Markatos, Feedstock atomization effects on FCC riser reactors selectivity, Chem. Eng. Sci. 54 (1999) 5617–5625.
[15] G.C. Lopes, L.M. Rosa, M. Mori, J.R. Nunhez, W.P. Martignoni, CFD study of industrial FCC risers: The effect of outlet configurations on hydrodynamics and reactions, Int. J. Chem. Eng. 2012 (2012).
[16] J.S. Buchanan, Analysis of heating and vaporization of feed droplets in fluidized catalytic cracking risers, Ind. Eng. Chem. Res. 33 (1994) 3104–3111.
[17] J. Gao, C. Xu, S. Lin, G. Yang, Y. Guo, Simulations of gas-liquid-solid 3-phase flow and reaction in FCC riser reactors, AIChE J. 47 (2001) 677–692.
[18] M.S. Van Buijtenen, N.G. Deen, S. Heinrich, S. Antonyuk, J.A.M. Kuipers, A discrete element study of wet particle-particle interaction during granulation in a spout fluidized bed, Can. J. Chem. Eng. 87 (2009) 308–317.
[19] C. Song, D. Liu, J. Ma, X. Chen, CFD-DEM simulation of flow pattern and particle velocity in a fluidized bed with wet particles, Powder Technol. 314 (2017) 346–354.
[20] B. Buck, S. Heinrich, Collision dynamics of wet particles: Comparison of literature models to new experiments, Adv. Powder Technol. 30 (2019) 3241–3252.
[21] R.H. Davis, E.J. Hinch, J.M. Serayssol, The elastohydrodynamic collision of two spheres, J. Fluid Mech. 163 (1986) 479–497.
[22] V.S. Sutkar, N.G. Deen, A.V. Patil, V. Salikov, S. Antonyuk, S. Heinrich, J.A. Kuipers, CFD-DEM model for coupled heat and mass transfer in a spout fluidized bed with liquid injection, Chem. Eng. J. 288 (2016) 185–197.
[23] F. Gollwitzer, I. Rehberg, C.A. Kruelle, K. Huang, Coefficient of restitution for wet particles, Phys. Rev. E - Statistical, Nonlinear, and Soft Matter Physics 86 (2012) 1–9.
[24] J. Shabanian, M.A. Duchesne, A. Runstedtler, M. Syamlal, R.W. Hughes, Improved analytical energy balance model for evaluating agglomeration from a binary collision of identical wet particles, Chem. Eng. Sci. 223 (2020) 115738.
[25] B. Buck, J. Lunewski, Y. Tang, N.G. Deen, J.A.M. Kuipers, S. Heinrich, Numerical investigation of collision dynamics of wet particles via force balance, Chem. Eng. Res. Des. 132 (2018) 1143–1159.
[26] O. Punch, M. Danczyk, M. Hawken, D.J. Holland, A comparison of pendulum experiments and discrete-element simulations of oblique collisions of wet spheres, AIChE J. 69 (2023).
[27] M. Wang, W. Zhu, Q. Sun, X. Zhang, A DEM simulation of dry and wet particle flow behaviors in riser, Powder Technol. 267 (2014) 221–233.
[28] M. Girardi, S. Radl, S. Sundaresan, Simulating wet gas-solid fluidized beds using coarse-grid CFD-DEM, Chem. Eng. Sci. 144 (2016) 224–238.
[29] J.E. Hilton, D.Y. Ying, P.W. Cleary, Modelling spray coating using a combined CFD-DEM and spherical harmonic formulation, Chem. Eng. Sci. 99 (2013) 141–160.
[30] S. Schmelzle, E. Asylbekov, B. Radel, H. Nirschl, Modelling of partially wet particles in DEM simulations of a solid mixing process, Powder Technol. 338 (2018) 354–364.
[31] F. Farivar, H. Zhang, Z.F. Tian, A. Gupte, CFD-DEM-DDM model for spray coating process in a Wurster Coater, J. Pharm. Sci. 109 (2020) 3678–3689.
[32] Z. Jiang, C. Rieck, A. Bück, E. Tsotsas, Modeling of inter- and intra-particle coating uniformity in a wurster fluidized bed by a coupled CFD-DEM-Monte Carlo approach, Chem. Eng. Sci. 211 (2020) 115289.
[33] H. Ali, S. Rohani, J.P. Corriou, Modelling and control of a riser type fluid catalytic cracking (FCC) unit, Chem. Eng. Res. Des. 75 (1997) 401–412.
[34] C. Derouin, D. Nevicato, M. Forissier, G. Wild, J.-R. Bernard, Hydrodynamics of riser units and their impact on FCC operation, Ind. Eng. Chem. Res. 36 (11) (1997) 4504–4515.
[35] Y. Tsuji, T. Tanaka, S. Yonemura, Cluster patterns in circulating fluidized beds predicted by numerical simulation (discrete particle model versus two-fluid model), Powder Technol. 95 (1998) 254–264,

[36] B.P.B. Hoomans, J.A.M. Kuipers, W.J. Briels, W.P.M. van Swaaij, Discrete particle simulation of bubble and slug formation in a two-dimensional gas-fluidised bed: A hard-sphere approach, Chem. Eng. Sci. 51 (1) (1996) 99–118.
[37] Y. Tang, S.H.L. Kriebitzsch, E.A.J.F. Peters, J.A.M. Kuipers, M.A. van der Hoef, A new drag correlation from fully resolved simulations of flow past monodisperse static arrays of spheres, AIChE J. 61 (2015) 688–698.
[38] J. Ramírez, M.J.A. de Munck, Z. Liu, D.R. Rieder, M.W. Baltussen, K.A. Buist, J.A.M. Kuipers, CFD-DEM evaluation of the clustering behavior in a riser the effect of the drag force model, Ind. Eng. Chem. Res. (2023).
[39] P.A. Cundall, O.D.L. Strack, A discrete numerical model for granular assemblies, Géotechnique 29 (1) (1979) 47–65.
[40] I. Yoon, S. Shin, Direct numerical simulation of droplet collision with stationary spherical particle: A comprehensive map of outcomes, Int. J. Multiph. Flow 135 (2021) 103503.
[41] H.V. Patel, S. Das, J.A.M. Kuipers, J.T. Padding, E.A.J.F. Peters, A coupled volume of fluid and immersed boundary method for simulating 3D multiphase flows with contact line dynamics in complex geometries, Chem. Eng. Sci. 166 (2017) 28–41.
[42] B. Freireich, C. Wassgren, Intra-particle coating variability: Analysis and Monte-Carlo simulations, Chem. Eng. Sci. 65 (2010) 1117–1124.
[43] W.I. Kariuki, B. Freireich, R.M. Smith, M. Rhodes, K.P. Hapgood, Distribution nucleation: Quantifying liquid distribution on the particle surface using the dimensionless particle coating number, Chem. Eng. Sci. 92 (2013) 134–145.
[44] A.E.C. Varas, E.A.J.F. Peters, J.A.M. Kuipers, Experimental study of full field riser hydrodynamics by PIV/DIA coupling, Powder Technol. 313 (2017) 402–416.
[45] N.G. Deen, S.H.L. Kriebitzsch, M.A. van der Hoef, J.A.M. Kuipers, Direct numerical simulation of flow and heat transfer in dense fluid-particle systems, Chem. Eng. Sci. 81 (2012) 329–344.
[46] K.A. Buist, L.J.H. Seelen, N.G. Deen, J.T. Padding, J.A.M. Kuipers, On an efficient hybrid soft and hard sphere collision integration scheme for DEM, Chem. Eng. Sci. 153 (2016) 363–373.
[47] S. Kamath, M.V. Masterov, J.T. Padding, K.A. Buist, M.W. Baltussen, J.A.M. Kuipers, Parallelization of a stochastic Euler-Lagrange model applied to large scale dense bubbly flows, J. Comp. Phys.: X 8 (2020).